

Surface reconstruction and directed electron transport in NiSe₂/MoSe₂ Mott-Schottky heterojunction catalysts promote urea-assisted water splitting

Xiaocheng Xu ^{a,1}, Haijun Liao ^{a,1}, Le Huang ^a, Sijie Chen ^a, Rui Wang ^a, Sheng Wu ^a, Yanxue Wu ^b, Zhipeng Sun ^{a,*}, Haitao Huang ^{c,*}

^a School of Materials and Energy, Guangdong University of Technology, Guangzhou 510006, Guangdong, China

^b Analysis and Test Center, Guangdong University of Technology, Guangzhou 510006, Guangdong, China

^c Department of Applied Physics, The Hong Kong Polytechnic University, Hung Hom, Hong Kong, China



ARTICLE INFO

Keywords:

Urea oxidation reaction
Hydrogen evolution reaction
Mott-Schottky heterojunction
Surface reconstruction
Directed electron transport

ABSTRACT

The construction of cost-effective electrocatalysts with remarkable activity and durability for the urea oxidation reaction (UOR) is urgently needed to achieve sustainable hydrogen production. Herein, a three-dimensional (3D) nanostructure with uniform NiSe₂/MoSe₂ Mott-Schottky heterojunction nanoneedle arrays densely grown on carbon cloth was designed and fabricated by a hydrothermal method followed by selenization treatment. In the UOR process, NiSe₂/MoSe₂ undergoes surface reconstruction into a Mo-NiOOH/NiSe₂ composite structure, and Mo-doping can optimize the adsorption/desorption of UOR intermediates. In the hydrogen evolution reaction (HER) process, the directed electron transfer brought by the Mott-Schottky heterojunction can modulate the electronic structure and optimize the d-band center, thus promoting HER. The well-designed NiSe₂/MoSe₂ as a bifunctional catalyst for urea-assisted electrolysis can reach 10 mA cm⁻² at only 1.44 V with almost no performance degradation for 48 h. This work provides a promising avenue to develop efficient HER/UOR bifunctional catalysts toward urea-assisted water electrolysis.

1. Introduction

Hydrogen (H₂) is a clean and non-polluting green energy carrier with no carbon emissions and high energy density, while the production of hydrogen from water electrolysis is of wide interest due to its environmental friendliness [1–3]. However, it is limited by the slow kinetics of the anode oxygen evolution reaction (OER), making the overall energy conversion inefficient [4]. This limitation can be addressed by oxidizing other more easily oxidized molecules, such as ethanol [5], glucose [6], and urea [7]. Among them, urea is of interest due to its abundance, low price, and non-combustibility [8,9]. The use of the urea oxidation reaction (UOR) instead of the thermodynamically slow OER can reduce the potential from 1.23 to 0.37 V [10]. In addition, industrial wastewater and domestic wastewater contain large amounts of urea, so urea electrolysis also offers a potential solution to water pollution problems [8].

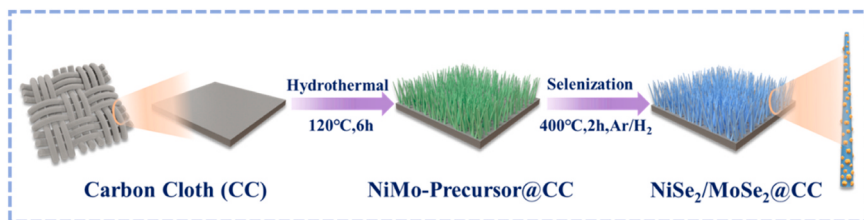
Noble metal-based catalysts (such as Pt, Ir, and Ru) are well known

for their high catalytic activity, but their inherent high cost and scarcity prevent them from being used in large-scale applications [11,12]. After years of research, many non-precious metal-based catalysts have been developed for UOR/OER/HER, such as phosphides [13,14], sulfides [15,16], oxides [17,18], selenides [19,20], etc. However, they are often available as a single catalyst, and do not possess high activity for both HER and OER/UOR, which increases the cost and complexity of electrolysis. In addition, the UOR reaction can be expressed as CO(NH₂)₂ + 6OH⁻ → N₂ + 5H₂O + CO₂ [9,21]. It is a complex process of six-electron transfer process, with multiple reaction pathways and slow kinetics, so it is of interest to elucidate its reaction mechanism [22,23]. Many studies have proved that sulfides, selenides, and phosphides are used as pre-catalysts for OER, in practice, the material surfaces are usually reconstructed into metal hydroxides (e.g. NiOOH, CoOOH), which participate in the reaction as the actual catalytic active sites for OER [24–27]. However, there is few research on the surface reconstruction phenomenon in UOR. Therefore, it is crucial to have a deep

* Corresponding authors.

E-mail addresses: zpsunxj@gdut.edu.cn (Z. Sun), aphuang@polyu.edu.hk (H. Huang).

¹ These authors contributed equally to this work.



Scheme 1. Synthesis process for NiSe₂/MoSe₂ on carbon cloth.

understanding of the surface reconstruction phenomenon in the UOR process to improve the catalytic activity of catalysts. Among many modification strategies, Mott-Schottky heterojunction engineering has received particular attention due to its ability to enable the directional movement of electrons within the catalyst, such as Ni/W₅N₄ [25], NiS/MoS₂ [28], CoS₂/MoS₂ [29], and CoMn/CoMn₂O₄ [30]. The built-in electric field in the Mott-Schottky heterojunction allows electrons to move directionally, creating electron-rich and electron-poor regions. On the one hand, this promotes OH⁻ adsorption in the electron-poor region, which facilitates the production of oxide/hydroxide active species in OER/UOR [31,32]. On the other hand, it can adjust the electronic structure and optimize the adsorption energy of hydrogen in HER [33,34]. Therefore, the construction of Mott-Schottky has emerged as an excellent method to well meet the design

requirements of efficient UOR/HER bifunctional catalysts.

In this work, we designed and synthesized a 3D nanostructure with uniform NiSe₂/MoSe₂ Mott-Schottky heterojunction nanoneedle arrays tightly grown on carbon cloth, which is used as a self-supported electrode for the highly efficient UOR and HER. Typically, the in-situ growth of nanoneedle arrays of NiSe₂/MoSe₂ not only promotes the mass transport, but also accelerates the bubble release, exposing more active sites to participate in the reaction. In the UOR process, the Mott-Schottky heterojunction promotes the surface reconstruction of NiSe₂/MoSe₂ to form a Mo-NiOOH/NiSe₂ composite structure, so that Mo-NiOOH participates in UOR as the actual active site. The results show that Mo doping can optimize the adsorption/desorption of UOR intermediates. In the HER process, the directed electron transfer generated by the Mott-Schottky heterojunction can modulate the electronic

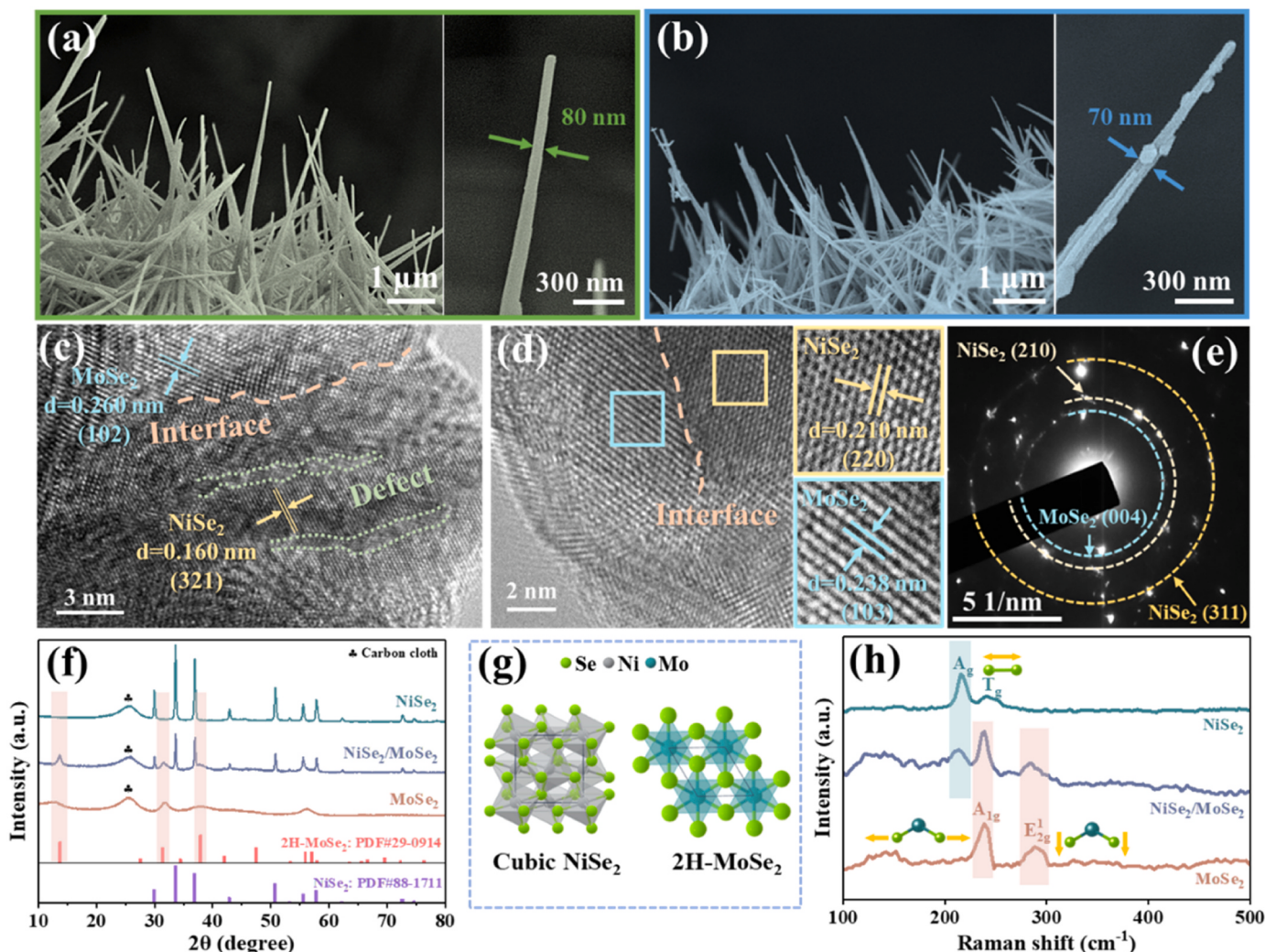


Fig. 1. SEM images of (a) NiMo-Pre and (b) NiSe₂/MoSe₂ (insets: high magnification SEM images). (c, d) HRTEM images and (e) SAED pattern of NiSe₂/MoSe₂ (insets of d: enlarged image of the corresponding region). (f) XRD patterns, (g) crystal structure models and (h) Raman spectra of NiSe₂, MoSe₂ and NiSe₂/MoSe₂.

structure and optimize the d-band center, thus promoting HER. The prepared NiSe₂/MoSe₂ exhibited excellent catalytic activities for UOR ($E_{10} = 1.34$ V) and HER ($E_{10} = 79$ mV) and required only 1.44 V to reach 10 mA cm^{-2} when used as a bifunctional catalyst for urea-assisted water electrolysis while maintaining almost no performance degradation over 48 h.

2. Experimental

2.1. Materials characterization

The phase composition and crystal structure of the material were characterized by X-ray diffraction (XRD, Rigaku, D/Max-III, Cu K α radiation) and Raman spectrometer (LabRAM HR Evolution, HORIBA Jobin Yvon, 532 nm laser). The microscopic morphology and structure of catalysts were characterized by field emission scanning electron microscope (FESEM, SU8010, Hitachi) and transmission electron microscope (TEM, Talos F200S, FEL). X-ray photoelectron spectroscopy (XPS) was recorded on a Thermo Fisher Escalab 250Xi with a monochromatic Al K α source. Electron Paramagnetic Resonance (EPR) spectra were collected using the Bruker EMX PLUS.

2.2. Synthesis of catalysts

To begin, a piece of carbon cloth (named CC, 2 × 3 cm, WOS1002, CeTech Co., Ltd.) and 3 ml of nitric acid (HNO₃, 65%, Guangzhou Chemical Reagent Factory Co., Ltd.) were placed in a 50 ml Teflon autoclave and maintained at 150 °C for 2 h. After cooling to ambient temperature, the CC was immersed in deionized water (DW) and anhydrous ethanol (C₂H₆O, 99.5%, Tianjin Damao Chemical Reagent Factory) for 15 min each. After drying, a clean CC was produced.

A piece of clean CC was immersed in 25 ml solution containing 1.5 mmol Nickel(II) nitrate hexahydrate [Ni(NO₃)₂·6H₂O, Guangzhou Chemical Reagent Factory Co. Ltd] and 1.5 mmol sodium molybdate dihydrate (Na₂MoO₄·2H₂O, Shanghai Aladdin Biochemical Technology Co. Ltd), which was heated to 150 °C for 6 h in a 50 ml Teflon autoclave. After that, the NiMo-Precursor@CC (named as NiMo-Pre) was obtained. Then a piece of NiMo-Pre and an appropriate amount of selenium powder (Se, Shanghai Aladdin Biochemical Technology Co. Ltd) were placed on the downstream and upstream side of the porcelain boat, respectively, and heated to 400 °C for 2 h with a heating rate of 5 °C min⁻¹ in an Ar/H₂ atmosphere. After cooling down to room temperature, the NiSe₂/MoSe₂ @CC (named as NiSe₂/MoSe₂) sample was obtained. The preparation methods of NiSe₂ and MoSe₂ were described in the Supporting Information.

2.3. Electrochemical measurements

Electrochemical testing of all samples was performed on a CHI 660E electrochemical workstation using a standard three-electrode system. UOR tests were performed in 1 M KOH and 0.5 M urea with the prepared catalyst material as the working electrode (1 × 1 cm²), a graphite rod as the counter electrode, and an Hg/HgO electrode as the reference electrode. HER and OER tests were performed under the same conditions except that the electrolyte was changed to 1 M KOH. All potentials were corrected to the reversible hydrogen electrode (RHE) by the following equation:

$$E_{(\text{RHE})} = E_{(\text{Hg/HgO})} + 0.098 \text{ V} + 0.059 \times \text{pH}.$$

N₂ was aerated into the electrolyte for 20 min before the start of the test, and 20 cyclic voltammetry (CV) cycles were performed at 50 mV/s for electrocatalyst activation. Linear sweeping voltammetry (LSV) was used to obtain the polarization curves at 2 mV/s and 85% iR-compensation was performed. CV cycles at different scan rates in the non-Faradic region (0.08–0.18 V vs. RHE and 0.73–0.83 V vs. RHE) are

used to estimate the double-layer capacitance (C_{dl}). The Electrochemical Impedance Spectroscopy (EIS) was performed on the electrocatalyst at a constant potential (−0.12 V vs. RHE and 1.38 V vs. RHE) from 10⁵ Hz to 10^{−2} Hz with an amplitude of 5 mV.

3. Results and discussion

3.1. Preparation and characterization of electrocatalysts

The preparation process of the NiSe₂/MoSe₂@CC electrocatalyst is shown in Scheme 1. First, the needle-like NiMo-precursor (NiMo-Pre) was grown on carbon cloth by hydrothermal method. The NiMo-pre was then converted to NiSe₂/MoSe₂ in situ by selenization in a tube furnace. In addition, MoSe₂ and NiSe₂ were prepared as control samples by controlled addition of nickel and molybdenum sources. In Figs. 1a and S1, the NiMo-pre with nanoneedle arrays grew on the originally smooth carbon cloth after hydrothermal treatment. The surface of the nanoneedles is exceedingly smooth, and their diameter is approximately 80 nm. After the selenization treatment (Fig. 1b), NiSe₂/MoSe₂ still maintained the morphology of the precursor nanoneedle arrays, with the front ends of the nanoneedles being sharper and the diameter of the nanoneedles are about 70 nm. Furthermore, a few nanoparticles appeared on the surface of the nanoneedles, and this change in morphology further increased the surface area of the catalyst. The EDS results show the mass ratio of Ni, Mo, and Se elements is approximately 1:1.5:5 (Fig. S2). The SEM images of NiSe₂ and MoSe₂ are shown in Fig. S3. TEM and high-resolution TEM (HRTEM) images of NiSe₂/MoSe₂ were collected to further examine the structure and composition of the catalyst. Fig. S4a shows that the NiSe₂/MoSe₂ are nanoneedles decorated with nanoparticles, which coincides with the SEM. As shown in Fig. 1c, lattice spacings of 0.260 nm and 0.160 nm can be observed, corresponding to the (102) and (321) planes of MoSe₂ and NiSe₂, respectively, with a clear interface between them. It is noteworthy that many defects (lattice distortions) appear inside the catalyst (Figs. 1c and S4b-d), which may be caused by space charges near the interface at the Mott-Schottky heterojunction [33,35]. The presence of defects is similarly demonstrated by EPR tests in Fig. S5 (EPR signal at g = 2.003 is associated with Se vacancies) [36]. In addition to this, clear interfaces can be observed between the (220) plane of NiSe₂ and the (103) plane of MoSe₂ (Fig. 1d). The selected area electron diffraction (SAED) patterns are also used for illustrating the crystal characteristics of NiSe₂/MoSe₂ (Fig. 1e). The diffraction rings corresponding to the (004) plane of MoSe₂ and the (311) and (210) planes of NiSe₂ can be observed. The TEM results showed that the prepared NiSe₂/MoSe₂ is rich in interfaces and defects, which facilitate the adsorption of reactants such as OH[−] and urea molecules and accelerate charge transfer, thus promoting the reaction kinetics [24,37].

Fig. 1f shows the XRD patterns of NiSe₂/MoSe₂, where the diffraction peaks at 29.9°, 33.6°, 36.9°, 42.9°, 50.7°, 55.5°, and 57.8° correspond to (200), (210), (211), (220), (311), (023) and (321) planes, respectively, of cubic NiSe₂ (PDF #88-1711). In addition, the XRD pattern of NiSe₂/MoSe₂ also shows diffraction peaks at 13.7°, 31.4° and 37.9°, corresponding to the (002), (100), and (103) planes of 2H-MoSe₂ (PDF #29-0914), respectively, indicating the presence of both cubic NiSe₂ and 2H-MoSe₂. In addition, we explore the effects of different selenization temperatures on material preparation (Fig. S6). Fig. 1g shows the crystal structure models of cubic NiSe₂ and 2H-MoSe₂. Further evidence of the phase composition is given by Raman spectra (Fig. 1h), where the characteristic peak of NiSe₂/MoSe₂ located at 214 cm^{−1} corresponds to the A_g mode of Se-Se stretching in NiSe₂ [38], and the characteristic peaks at 237 and 285 cm^{−1} correspond to the out-of-plane A_{1g} mode and in-plane E_{2g}¹ mode in 2H-MoSe₂, respectively [39]. Based on the results of TEM, XRD, and Raman, it can be concluded that the NiSe₂/MoSe₂ heterostructured catalyst contains both NiSe₂ and 2H-MoSe₂ phases. NiSe₂ and 2H-MoSe₂ are typical metal and semiconductor in selenides, respectively (Fig. S7) [40,41]. According to the solid-state

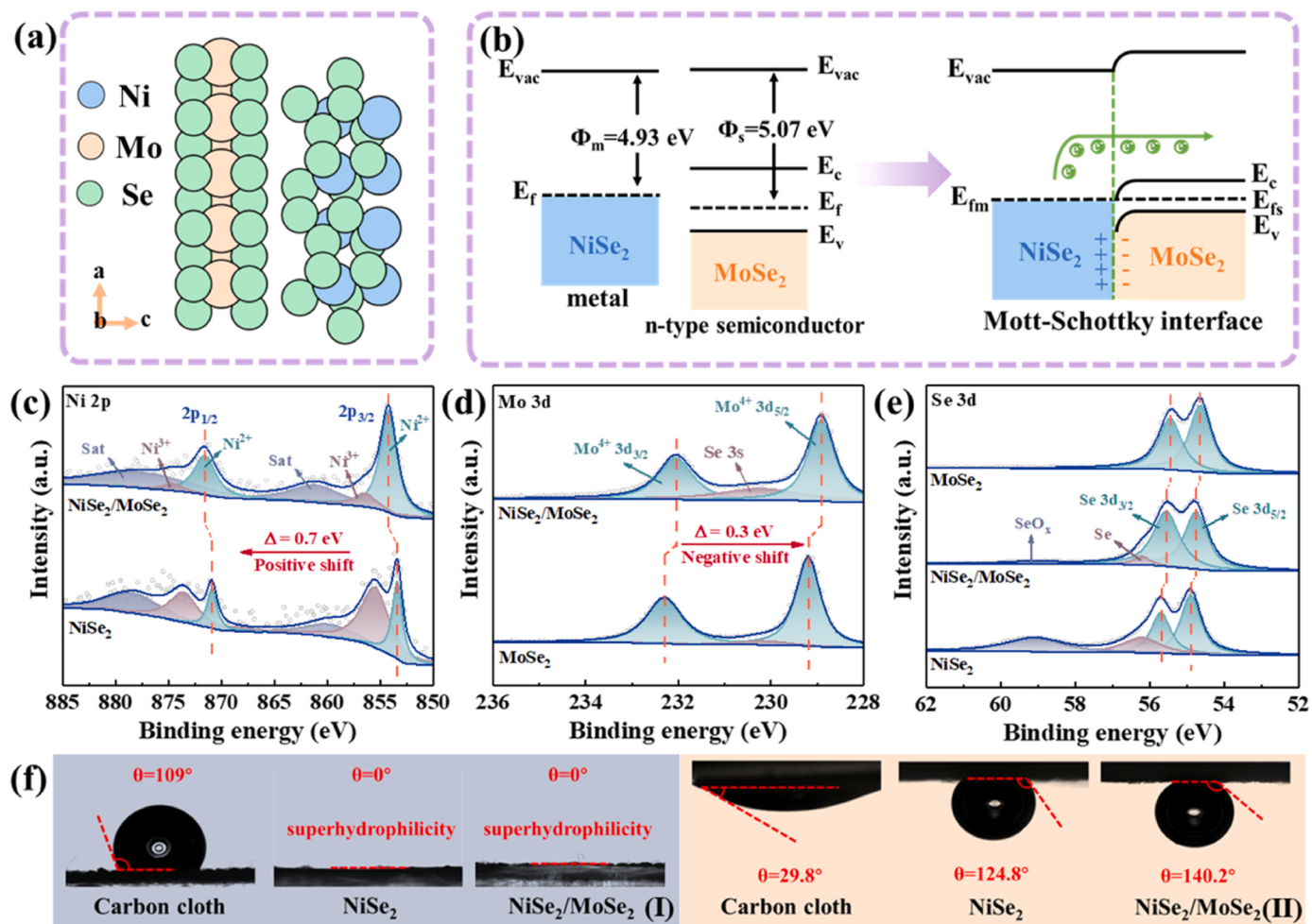


Fig. 2. (a) Crystal structure model of NiSe₂/MoSe₂. (b) The energy band diagrams of metallic NiSe₂ and n-type semiconductor MoSe₂ before and after the formation of Mott-Schottky heterojunction. (c) Ni 2p, (d) Mo 3d and (e) Se 3d XPS spectra of NiSe₂, MoSe₂ and NiSe₂/MoSe₂. (f) The droplet contact angle images (I) and the bubble contact angle images (II) of the carbon cloth, NiSe₂ and NiSe₂/MoSe₂.

physics theory, the contact of metal and semiconductor can form a Mott-Schottky heterojunction with a built-in electric field [33,34]. The crystal structure models of NiSe₂, 2H-MoSe₂, and NiSe₂/MoSe₂ are shown in Figs. S8 and 2a. According to the density functional theory (DFT) results (Fig. S9), the work functions of metallic NiSe₂ and semiconductor MoSe₂ are 4.93 and 5.07 eV, respectively, which satisfy the conditions for constructing Mott-Schottky heterojunction (Fig. 2b). When NiSe₂ and MoSe₂ come into contact to form a heterostructure, electrons will spontaneously flow from NiSe₂ to MoSe₂. This results in a built-in electric field that can accelerate electron transport and regulate the adsorption of catalytic reaction intermediates, thus facilitating the catalytic reaction [28–30,42].

In order to study the surface chemical components and electronic interactions of catalysts, XPS was conducted to investigate the interaction between NiSe₂ and MoSe₂ in NiSe₂/MoSe₂. The overall XPS spectra of NiSe₂/MoSe₂ show the signals of the Ni, Mo, and Se elements (Fig. S10). In the Ni 2p region (Fig. 2c), the peaks of NiSe₂ at 853.5 and 870.9 eV are attributed to Ni²⁺ 2p_{3/2} and Ni²⁺ 2p_{1/2} in pure NiSe₂ [43]. The peaks at 855.6 and 873.7 eV with a pair of satellite peaks (860.0 and 878.7 eV) correspond to nickel oxides [44]. After hybridization with MoSe₂, the binding energies of Ni²⁺ 2p and Ni³⁺ 2p in NiSe₂/MoSe₂ exhibit a positive shift of about 0.7 eV, indicating a charge transfer caused by electronic interaction. In contrast, the Mo 3d peaks of NiSe₂/MoSe₂ shift by about 0.3 eV to lower energies than pure MoSe₂ at 229.2/232.3 eV (Fig. 3d). Moreover, the Se 3d peaks of NiSe₂/MoSe₂ also show a small shift compared with pure NiSe₂ and MoSe₂ (Fig. 3e).

Thus, the XPS results clearly show the electron transfer from NiSe₂ to MoSe₂, further demonstrating the formation of NiSe₂/MoSe₂ Mott-Schottky heterojunction. It is known that the hydrophilicity of the catalyst determines whether the surface active sites are better exposed to the electrolyte [45]. Besides, the accumulation of bubbles on the catalyst surface leads to a "bubble shielding effect", which inhibits the contact between the electrolyte and the catalyst [46,47]. Therefore, the design of catalysts with excellent hydrophilicity and aerobic properties would facilitate the HER and UOR processes. As shown in Fig. 2f I, compared with the large water contact angle of carbon cloth (109°), the prepared NiSe₂ and NiSe₂/MoSe₂ are superhydrophilic with a water contact angle close to 0°. Moreover, NiSe₂/MoSe₂ shows the largest underwater contact angle of 140.2° compared with carbon cloth (0°) and NiSe₂ (124.8°), indicating its good aerobic properties (Fig. 2f II). In summary, the prepared NiSe₂/MoSe₂ has the optimal hydrophilic and aerobic properties, which not only makes the catalyst surface in close contact with the electrolyte but also better reduces the bubble adhesion, thus facilitating the catalytic reaction.

3.2. UOR and HER performance

The electrochemical performance of the prepared electrocatalysts was tested in the electrolyte (1 M KOH + 0.5 M Urea or 1 M KOH) using a standard three-electrode system for investigating the effect of heterostructure on the UOR performance. As shown in Fig. S11, NiSe₂/MoSe₂ at 400 °C exhibits optimal UOR performance. From the LSV curves of

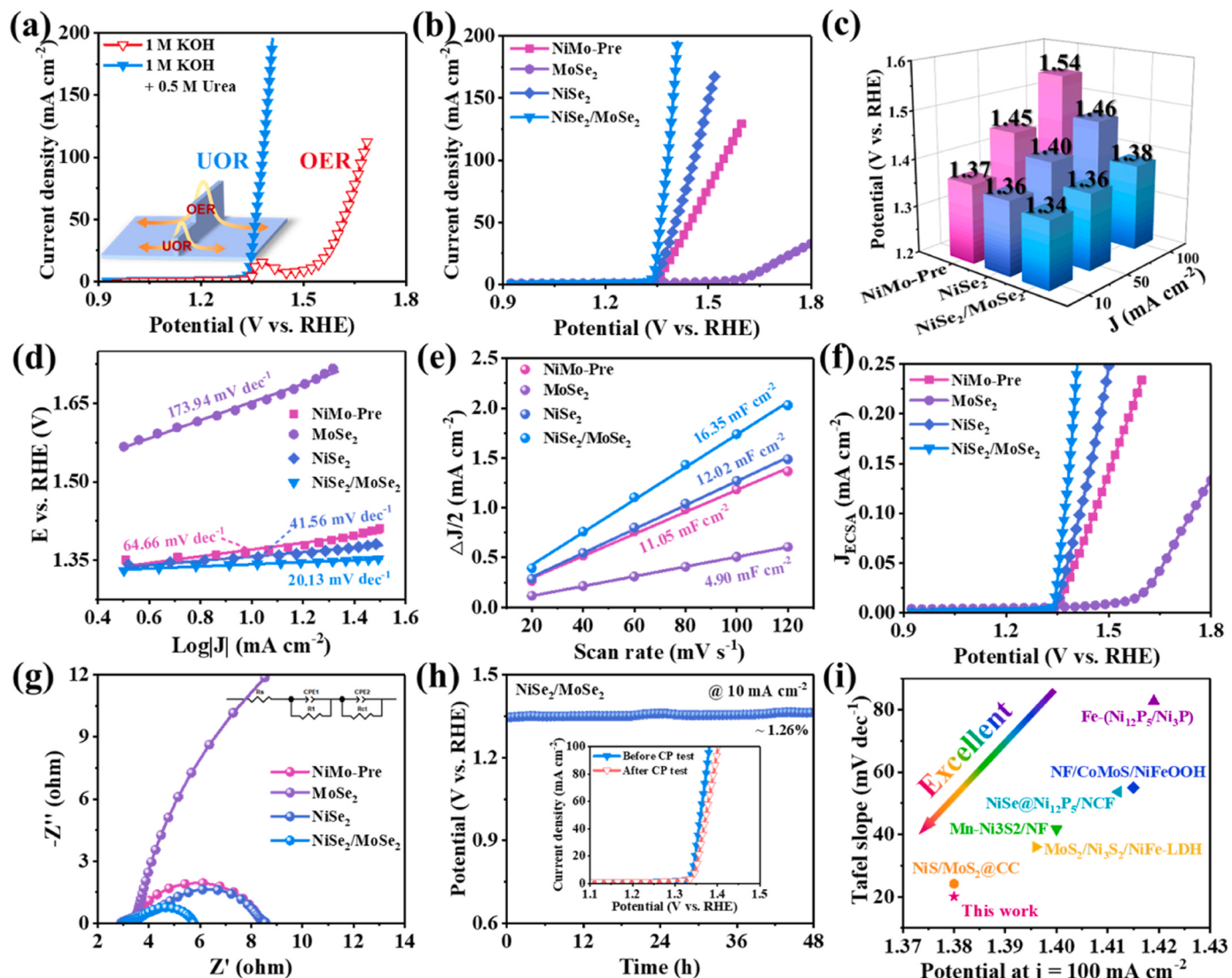


Fig. 3. (a) Comparison of the OER and UOR polarization curves of NiSe₂/MoSe₂. (b) The UOR polarization curves of NiMo-Pre, MoSe₂, NiSe₂ and NiSe₂/MoSe₂. (c) Overpotentials of NiMo-Pre, NiSe₂ and NiSe₂/MoSe₂ at 10, 50 and 100 mA cm^{-2} . (d) Tafel plots, (e) C_{dl} values, (f) LSV curves normalized by ECSA and (g) Nyquist plots of NiMo-Pre, MoSe₂, NiSe₂ and NiSe₂/MoSe₂ (inset: equivalent circuit diagram). (h) CP curves of NiSe₂/MoSe₂ for UOR (inset: LSV curves before and after the CP test of NiSe₂/MoSe₂). (i) Comparison of the UOR potential at 100 mA cm^{-2} and Tafel slopes of NiSe₂/MoSe₂ with those of recently reported UOR electrocatalysts.

OER and UOR of NiSe₂/MoSe₂ in Fig. 3a, it is obvious that after adding urea to the electrolyte, a sharply rising current at a lower potential is observed for NiSe₂/MoSe₂, and the results indicate that energy-efficient hydrogen production can be achieved at lower potentials by replacing OER with UOR. In addition, NiSe₂/MoSe₂ demonstrates optimal UOR performance in comparison with other comparative samples, achieving greater current density at the same potential (Fig. 3b and c). For example, NiSe₂/MoSe₂ requires only 1.34 V to reach 10 mA cm^{-2} , which is lower than that of NiSe₂ (1.36 V), MoSe₂ (1.65 V), and NiMo-Pre (1.37 V). Notably, many studies have shown that NiOOH species have been recognized as the primary sources for the UOR [22,23], so MoSe₂ exhibits poor performance compared with the samples containing elemental Ni. Similarly, the Tafel slope of NiSe₂/MoSe₂ is 20.13 mV dec⁻¹ (Fig. 3d), which is smaller than that of NiSe₂ (41.56 mV dec⁻¹), MoSe₂ (173.94 mV dec⁻¹) and NiMo-Pre (64.66 mV dec⁻¹), indicating that the formation of heterostructure can significantly accelerate the UOR kinetics. The electrochemically active surface area (ECSA) is a very critical index in the assessment of electrocatalytic activity, which is estimated by calculating C_{dl} from CV curves at different sweep rates (Fig. S12). In Fig. 3e, the C_{dl} value of NiSe₂/MoSe₂ is calculated as 30.33

mF cm⁻², which is significantly larger than that of NiSe₂ (24.05 mF cm⁻²), MoSe₂ (9.80 mF cm⁻²) and NiMo-Pre (22.09 mF cm⁻²), showing that NiSe₂/MoSe₂ has more exposed active sites for the UOR. To gain insight into the intrinsic activity of the electrocatalyst, the ECSA normalized LSV curves, turnover frequency (TOF), and mass activity (MA) were also investigated. As shown in Fig. 3f, the NiSe₂/MoSe₂ exhibits a larger normalized current density at the same potential, further indicating that the heterostructure is essential in enhancing the UOR performance. Similarly, the TOF and MA results further confirm that NiSe₂/MoSe₂ has optimal UOR intrinsic activity (Fig. S13).

The charge transfer kinetics of the electrocatalysts were evaluated by EIS (Figs. 3g and S14). The charge-transfer resistance (R_{ct}) value of NiSe₂/MoSe₂ is 2.5 Ω , which is smaller than the values of NiSe₂ (4.3 Ω), MoSe₂ (47.5 Ω), and NiMo-Pre (4.8 Ω), indicating that NiSe₂/MoSe₂ has the best electron transfer efficiency in the electrochemical process. One of the most important metrics for assessing the effectiveness of electrocatalysts is their long-term stability. As shown in the CP test results (Fig. 3h), NiSe₂/MoSe₂ can be maintained at 10 mA cm^{-2} for 48 h with almost no degradation of performance. And it can also maintain good UOR performance after 36 h at 100 mA cm^{-2} (Fig S15). The prepared

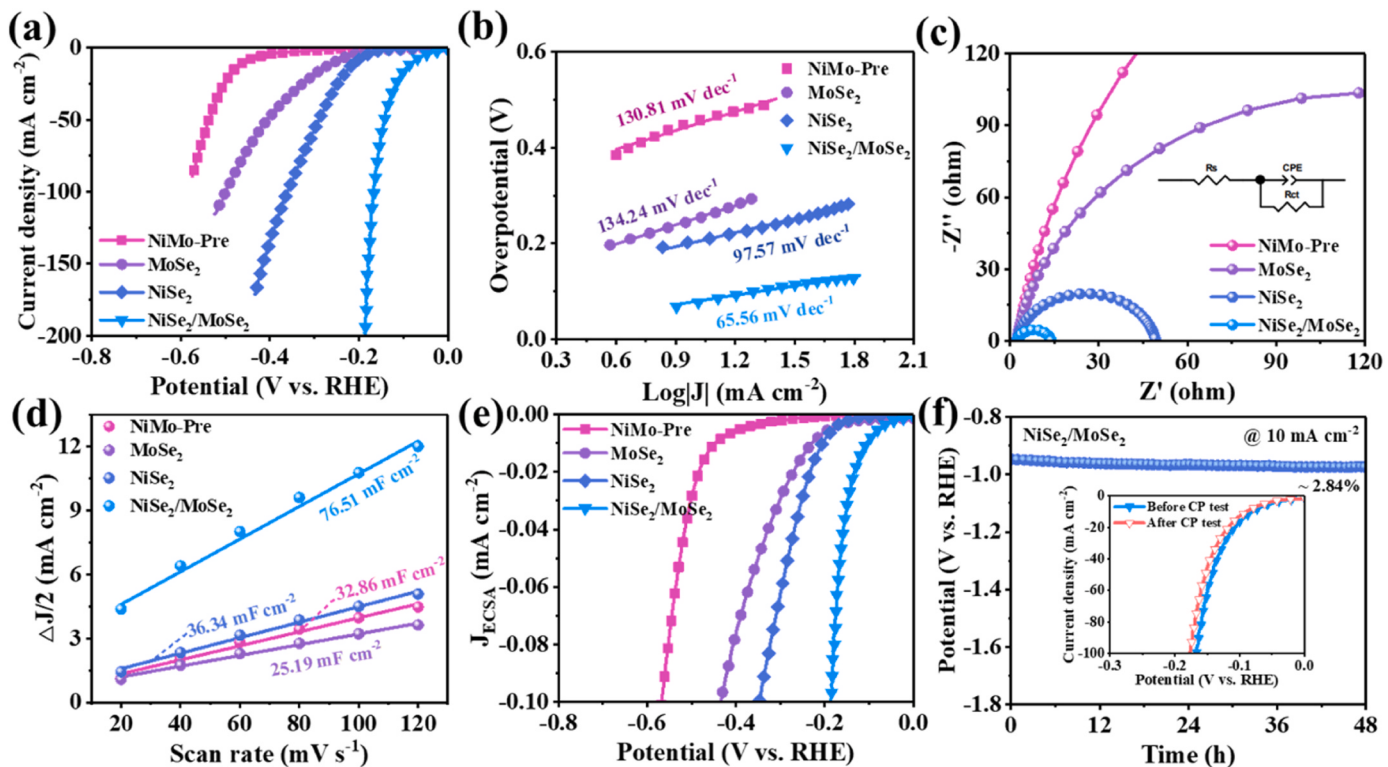


Fig. 4. (a) The HER polarization curves, (b) Tafel plots, (c) Nyquist plots (inset: equivalent circuit diagram), (d) C_{dl} values, and (e) LSV curves normalized by ECSA of NiMo-Pre, MoSe₂, NiSe₂ and NiSe₂/MoSe₂. (f) CP curves of NiSe₂/MoSe₂ for HER (inset: LSV curves before and after the CP test of NiSe₂/MoSe₂).

NiSe₂/MoSe₂ exhibited excellent UOR performance compared with similar catalysts reported recently (Fig. 3i and Table S1). In addition, we explored the effect of urea content on UOR performance (Fig. S16a). It can be seen that with the increase of urea content, the oxidation peak gradually becomes larger, and when the urea content exceeds 0.3 M, the oxidation peak gradually disappears, which means that UOR replaces OER. At the same time, NiSe₂/MoSe₂ also showed good UOR performance in alkaline real urine (Fig. S16b).

The cathodic reaction is also crucial in urea electrolysis. Therefore, the HER performance of the prepared electrocatalysts was further tested in 1 M KOH solution. As shown in Fig. S11, NiSe₂/MoSe₂ at 400 °C exhibits optimal HER performance. As observed from the HER polarization curves in Fig. 4a, the NiSe₂/MoSe₂ shows the best HER performance with an overpotential of only 79 mV to reach 10 mA cm⁻², compared with 459, 256, and 209 mV for NiMo-Pre, MoSe₂, and NiSe₂, respectively. Similarly, NiSe₂/MoSe₂ exhibits the optimal Tafel slope (65.56 mV dec⁻¹) compared with other samples (Fig. 4b), indicating that the formation of heterostructure can effectively improve the kinetics of the HER process. Moreover, the excellent HER performance is also inseparable from the fast charge transport, and the R_{ct} of NiSe₂/MoSe₂ is 2.01 Ω, smaller than NiMo-Pre (4.41 Ω), MoSe₂ (47.51 Ω), and NiSe₂ (2.73 Ω) (Figs. 4c and S17). As shown in Figs. 4d and S18, there is the largest C_{dl} value for NiSe₂/MoSe₂, showing that it exposes more active sites, while the optimal intrinsic activity is also indicated in the ECSA-normalized LSV curves (Fig. 4e). Another crucial sign of HER performance is the electrocatalyst's long-term stability. As shown in Fig. 4f, NiSe₂/MoSe₂ was able to hold at 10 mA cm⁻² for 48 h with almost no degradation in performance. And it can also maintain good HER performance after 36 h at 100 mA cm⁻² (Fig. S15). Meanwhile, SEM, XRD, and XPS data point out that the material does not change after the stability test (Figs. S19 and S20). Furthermore, NiSe₂/MoSe₂ also exhibited excellent performance compared with other transition metal selenides in Table S2.

3.3. Exploration of UOR and HER mechanisms

Transition metal sulfides, phosphides, and selenides are often considered pre-catalysts in OER/UOR and undergo surface reconstruction during the anodic reaction to generate species such as oxides/hydroxides that act as actual active sites [24,26,48]. The MoSe₂ in NiSe₂/MoSe₂ disappeared after a long-term UOR stability test (Fig. S21), but the phase of NiSe₂/MoSe₂ did not change after a long-term HER stability test (Fig. S20a). The phenomenon of MoSe₂ disappearance during UOR was investigated. Fig. S22 shows the CV scans for NiSe₂/MoSe₂ from 0 to 1.3 V vs. RHE. It can be seen that a larger oxidative peak appears in the first CV scan without a reductive peak, the oxidative peak becomes smaller in the second CV scan, and the oxidative peak disappears in the third CV scan, which demonstrates the surface reconstruction of NiSe₂/MoSe₂. As the anode potential increases, the metal elements are oxidized to a higher valence state. When Mo is oxidized to the +6 state, it becomes MoO₄²⁻ and diffuses into the alkaline electrolyte [49–51]. In order to explore the process of surface reconstruction of NiSe₂/MoSe₂ in UOR, the NiSe₂/MoSe₂ samples after the UOR stability test was further characterized. The dissolution of MoSe₂ leads to a large change in the morphology of NiSe₂/MoSe₂, and the originally regular nanoneedles become distorted and adhered to each other (Fig. S23). However, considering that MoSe₂ has almost no catalytic activity in UOR, its dissolution would actually favor the exposure of the active site and thus facilitate the UOR process [52]. The EDS data showed a significant reduction of Mo elements in NiSe₂/MoSe₂ after the UOR stability test (Fig. S23d), which also corroborated the dissolution of MoSe₂. XPS was conducted on NiSe₂/MoSe₂ and tested for UOR stability to study the surface chemical state of NiSe₂/MoSe₂ before and after surface reconstruction in the UOR. Compared with the initial sample, the area of the Ni³⁺ peak in the samples after UOR increased significantly (Fig. 5a), which was related to the production of NiOOH by the catalyst at a high potential for a long time. In Fig. 5b, after long-term UOR, the peak of Mo⁴⁺ disappeared and the peaks of Mo⁶⁺ (232.2/235.8 eV) and Mo

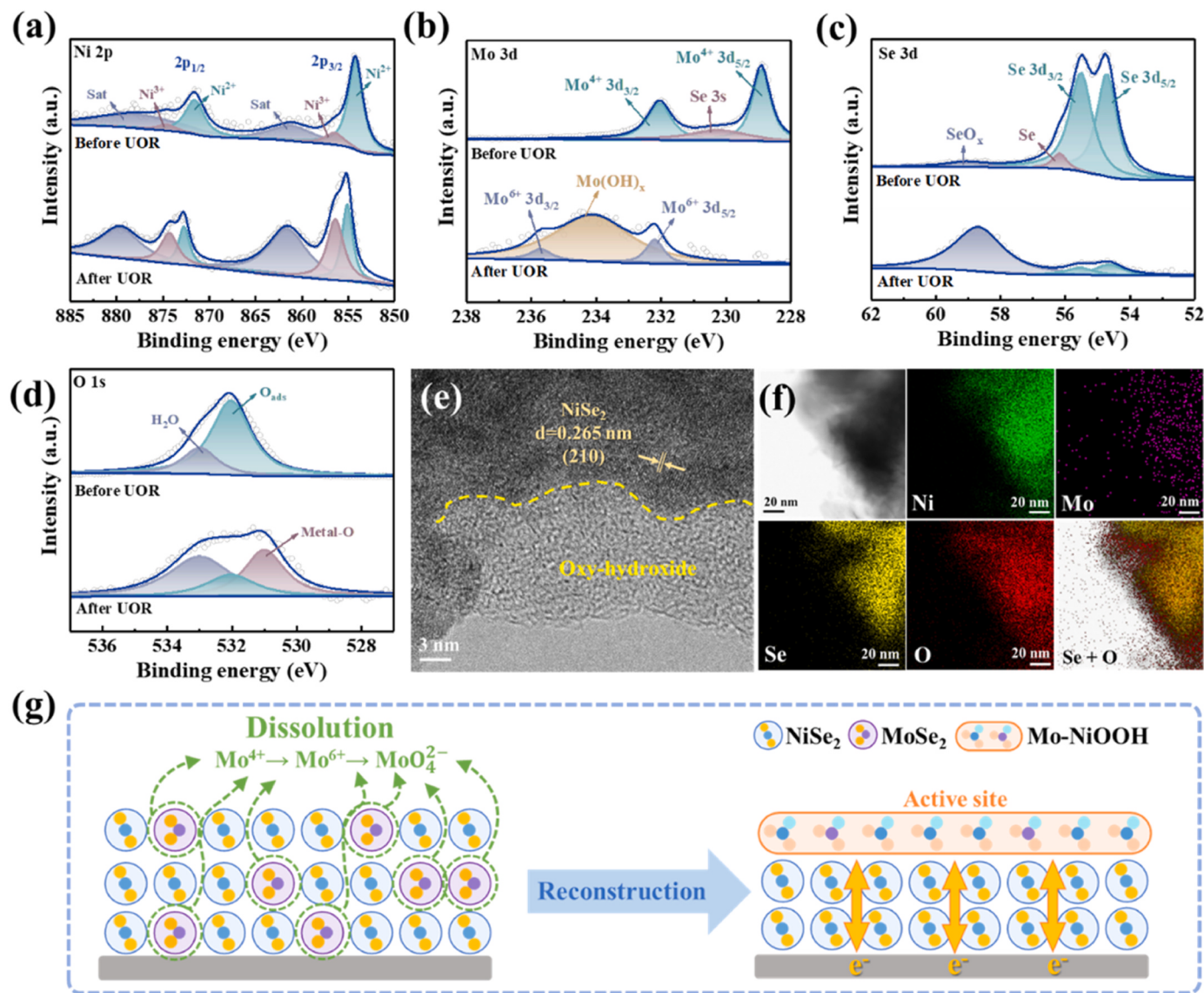


Fig. 5. (a) Ni 2p, (b) Mo 3d, (c) Se 3d, and (d) O 1s of NiSe₂/MoSe₂ before and after UOR. (e) HRTEM image and (f) TEM image and corresponding EDS elemental maps of NiSe₂/MoSe₂ after UOR stability test. (g) Schematic diagram of the surface reconstruction for NiSe₂/MoSe₂.

(OH)_x (234.1 eV) appeared due to the presence of MoO₄²⁻ and Mo(OH)_x species [49], which is consistent with the disappearance of MoSe₂ in XRD. Similarly, the peak area of SeO_x increases significantly in the Se 3d region after a long-term UOR (Fig. 5c). In Fig. 5d, the metal-O peak appears after UOR stability test in the spectrum of O 1s, which is associated with metal oxides/ oxyhydroxides [53,54]. As shown in the HRTEM images (Figs. 5e and S24), amorphous NiMo hydroxides are present at the edge of NiSe₂/MoSe₂ after a long UOR stability test. Additionally, as shown in Fig. 5f, the catalyst contains Ni, Se, O, and Mo elements after the UOR stability test, with more O than Se at the edge position, again demonstrating the presence of oxides/hydroxides at the edge of the catalyst.

In summary, the NiSe₂/MoSe₂ heterostructured catalyst undergoes surface reconstruction during the UOR process as shown in Fig. 5g. MoSe₂ is dissolved into the electrolyte as MoO₄²⁻ and SeO₄²⁻ (or SeO₃²⁻) ions at high potential, resulting in a core-shell structure with NiSe₂ inside and Mo-doped NiOOH outside. The internal NiSe₂ acts as a high-speed transport channel for electrons, and the external Mo-NiOOH acts as the actual active site in the UOR.

To investigate the reason for the high UOR activity of NiSe₂/MoSe₂, NiSe₂ and NiSe₂/MoSe₂ were further analyzed. An approximate linear

relationship between the peak anodic current density (I_{pa}) and the square root of the scan rate ($v^{1/2}$) was obtained from the CV curves in Fig. S25, which was used to evaluate the ability of the catalyst to generate NiOOH in situ. As shown in Fig. 6a, the slope of NiSe₂/MoSe₂ is higher than that of NiSe₂, indicating a better diffusion ability of OH on NiSe₂/MoSe₂, which is better for the in situ synthesis of NiOOH species [22]. Furthermore, the oxidation peak of NiSe₂/MoSe₂ occurs at a lower potential than that of NiSe₂ (Fig. S26), due to the fact that Mo promotes the conversion of Ni²⁺ to Ni³⁺ at a lower potential [55,56]. As can be seen in Figs. 6b and S27, the values of C_{dl} for NiSe₂ are the same in both electrolytes, while there is a significant difference in C_{dl} values for NiSe₂/MoSe₂, which represents that NiSe₂/MoSe₂ has more active sites involved in the UOR process after the addition of urea to the electrolyte.

DFT calculations were used to further investigate the underlying mechanism for the high UOR and HER activities of NiSe₂/MoSe₂. Due to the surface reconstruction of NiSe₂ and NiSe₂/MoSe₂, NiOOH and Mo-NiOOH (Fig. 6c) were selected during UOR process in this study. Figs. 6d and S28 show a typical UOR pathway [13,19], while the change of Gibbs free energy (ΔG) of each UOR step is used to reveal energy barrier. It can be seen that the rate-determining step (RDS) for NiOOH is the dehydrogenation step from CO(NH₂-N)* to CO(NH-N)*, while the

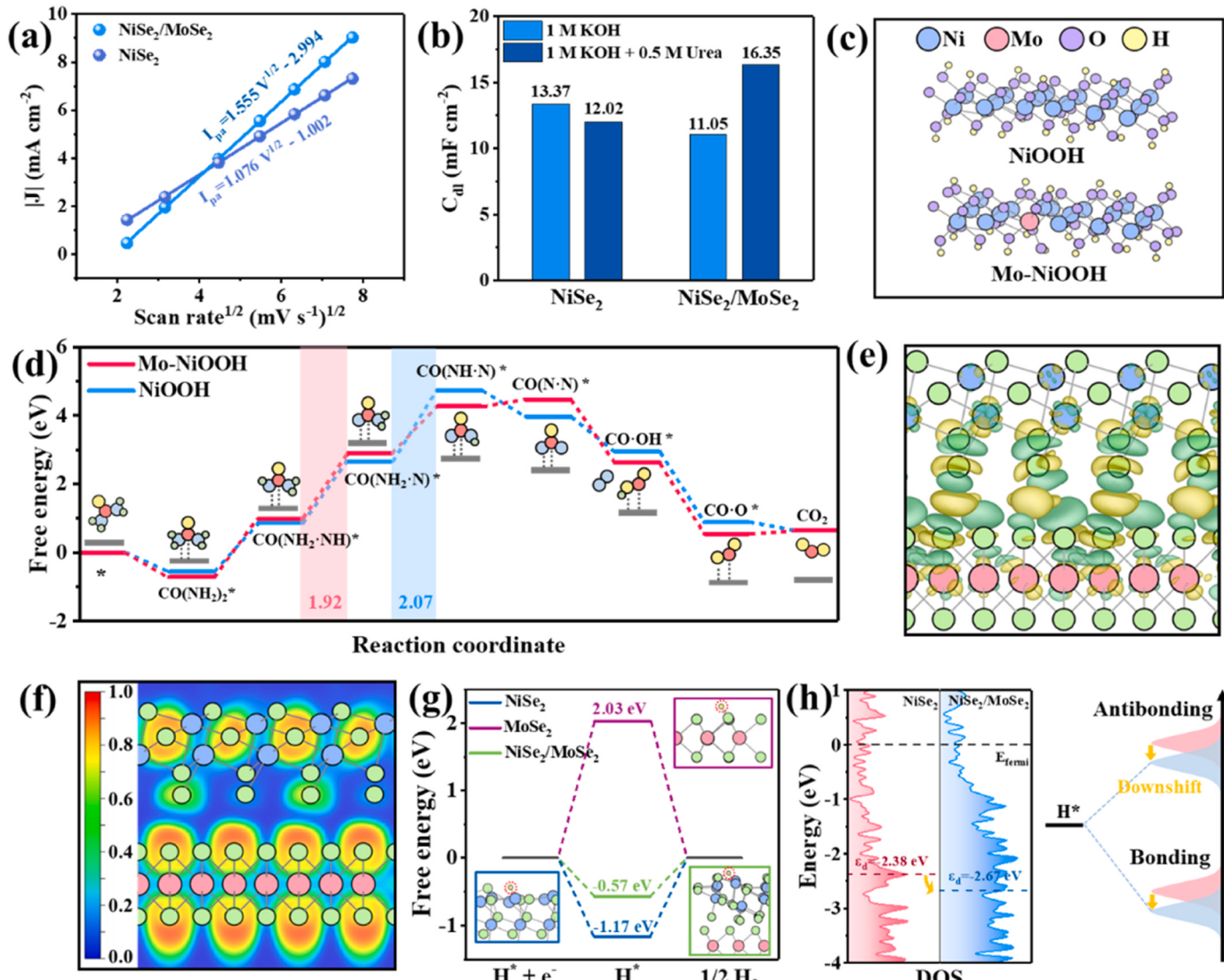


Fig. 6. (a) Linear relationship between the peak current density and the square root of the scan rate ($I_{\text{pa}} \sim v^{1/2}$) for NiSe_2 and $\text{NiSe}_2/\text{MoSe}_2$ in $1 \text{ M KOH} + 0.5 \text{ M Urea}$. (b) The C_{dl} values of NiSe_2 and $\text{NiSe}_2/\text{MoSe}_2$ in different electrolytes. (c) Theoretical structure models of NiOOH and Mo-NiOOH . (d) UOR energy pathways of NiOOH and Mo-NiOOH . (e) The charge density difference analysis of $\text{NiSe}_2/\text{MoSe}_2$. (Yellow and green represent electrons accumulation and depletion.) (f) Electron localization function image of $\text{NiSe}_2/\text{MoSe}_2$. (g) Gibbs free-energy diagrams of NiSe_2 , MoSe_2 and $\text{NiSe}_2/\text{MoSe}_2$ for H adsorption (H^*). (h) The density of states of NiSe_2 and $\text{NiSe}_2/\text{MoSe}_2$, and the schematic illustration of the bond formation between the catalyst surface and H^* . The d-band centers are also shown.

RDS for Mo-NiOOH is $\text{CO}(\text{NH}_2\text{-NH})^*$ to $\text{CO}(\text{NH}_2\text{-N})^*$. Also, the ΔG value of the RDS of Mo-NiOOH (1.92 eV) is smaller than that of NiOOH (2.07 eV), which represents that the Mo doping can reduce the activation energy of the RDS and facilitate the multi-step UOR process. And the Ni site is the active site in the UOR process for NiOOH and Mo-NiOOH .

In the HER process, the electrocatalyst did not undergo surface reconstruction, so MoSe_2 , NiSe_2 , and $\text{NiSe}_2/\text{MoSe}_2$ were analyzed. As shown in the charge density difference analysis of Fig. 6e, a strong electronic interaction between NiSe_2 and MoSe_2 indicates a charge redistribution between them. In addition, the electron localization function (ELF) (Fig. 6f) shows more electron aggregation on the MoSe_2 side, indicating electron transfer from NiSe_2 to MoSe_2 [57], which is consistent with the results of XPS and work function analysis. The rate of the HER process is inextricably linked to the adsorption and desorption of H on the catalyst surface and can be analyzed by calculating the ΔG_{H^*} at the different electrocatalysts. The closer the value of ΔG_{H^*} is to 0, the more favorable the HER process [28,58]. As shown in Fig. 6g, the ΔG_{H^*} of MoSe_2 is 2.03 eV, which represents a weaker H adsorption, while the

ΔG_{H^*} of NiSe_2 is -1.17 eV , which represents stronger adsorption and is not favorable for desorption. When MoSe_2 and NiSe_2 are combined, the ΔG_{H^*} of $\text{NiSe}_2/\text{MoSe}_2$ (-0.57 eV) is further optimized due to the synergistic effect of electron interaction and charge redistribution.

The electronic interaction between the adsorbate and the catalyst can be seen as the coupling between the adsorbate valence state and the transition metal d-states, resulting in the formation of separate bonding and anti-bonding states [59]. Since the energy of the bonding states is well below the Fermi energy level (E_f), they are usually completely filled, whereas the electronic filling of the anti-bonding states depends on these energy states relative to E_f and in turn affects the bond strength between the adsorbate and the catalyst [60]. The energy of antibonding states is always higher than that of D-states, so the adsorbate-metal interaction can be described by the d-band center (ε_d) model [57,58]. As shown in Fig. 6h, the ε_d values of NiSe_2 and $\text{NiSe}_2/\text{MoSe}_2$ are -2.38 eV and -2.67 eV , respectively, indicating that the ε_d is far from the E_f after the formation of the Mott-Schottky heterojunction. The downward shift of ε_d allows the antibonding state to be filled with more electrons, thus weakening the adsorption of H and promoting desorption, which is

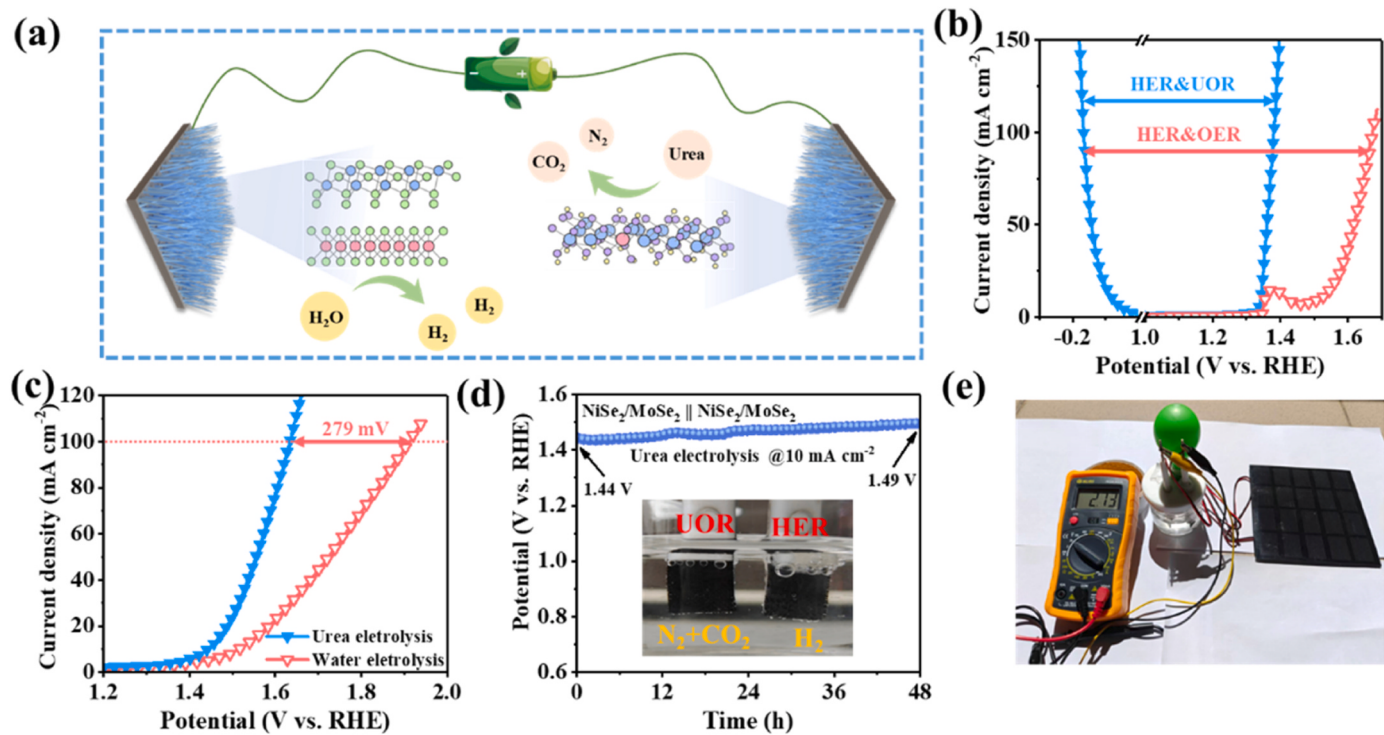


Fig. 7. (a) Schematic illustration of urea-assisted water splitting using NiSe₂/MoSe₂ as anode and cathode (b) Comparison of the HER, OER and UOR polarization curves of NiSe₂/MoSe₂. (c) Polarization curves of NiSe₂/MoSe₂ for overall water splitting and urea electrolysis. (d) CP curves of NiSe₂/MoSe₂ for urea electrolysis (inset: the digital photograph of H₂, N₂ and CO₂ bubbles evolving from the electrocatalyst). (e) Schematic diagram of urea-assisted water splitting driven by solar cell.

consistent with the results of ΔG_{H^*} .

3.4. Overall urea electrolysis performance

The excellent HER and UOR performance of NiSe₂/MoSe₂ inspired us to use it as electrode materials to build electrolytic cells (Fig. 7a and b). Two pieces of NiSe₂/MoSe₂ electrocatalysts were used as an anode and cathode, and 1 M KOH and 1 M KOH + 0.5 M urea were used as an electrolyte for water electrolysis and urea electrolysis. It is noteworthy that the HER activity of NiSe₂/MoSe₂ is almost unchanged in the 1 M KOH electrolyte with urea added, which represents its great potential in urea electrolysis (Fig. S29). The LSV curves of electrolytic urea show a significant thermodynamic and kinetic advantage over that of electrolytic water (Fig. 7c). Specifically, electrolytic water requires 1.913 V to reach 100 mA cm⁻², while electrolytic urea requires only 1.634 V. It indicates that by constructing heterostructure and using UOR instead of the slow OER the efficiency of hydrogen production can be greatly improved. Besides, the stability of the electrolytic cell was measured by the CP method (Fig. 7d), and the voltage was increased by only 0.05 V after holding a constant current density at 10 mA cm⁻² for 48 h, which demonstrated that the electrolytic cell composed of NiSe₂/MoSe₂ has excellent stability. In addition, the NiSe₂/MoSe₂ electrolyzer was connected in series with a solar cell to form a complete solar-powered urea-assisted water splitting device (Fig. 7e). As can be seen, the solar-powered electrolyzer is capable of continuous production of hydrogen to fill the balloon. In conclusion, the heterostructure of NiSe₂/MoSe₂ is an efficient bifunctional catalyst for UOR and HER, which provides an effective way for urea-assisted energy-saving hydrogen production.

4. Conclusions

We have designed and synthesized a Mott-Schottky heterojunction catalyst consisting of NiSe and 2 H-MoSe₂ on carbon cloth for urea-assisted hydrogen production, which has the morphology of nanoparticles on nanoneedles. This allows it to contact the electrolyte and

accelerate the bubble release while exposing more active sites to participate in the reaction. The results demonstrate that the Mott-Schottky heterojunction is able to promote electron-directed transport and surface reconstruction, enabling NiSe₂/MoSe₂ to exhibit excellent HER and UOR performance. The urea electrolysis using NiSe₂/MoSe₂ as a bifunctional catalyst can reach 10 mA cm⁻² at only 1.44 V, with almost no performance degradation for 48 h. The results of DFT have demonstrated that electron-directed transport modulates the d-band center and thereby optimizes the hydrogen adsorption energy, and the Mo-NiOOH produced by the surface reconstruction is capable of better adsorption and desorption of the reactants and products during the UOR process. These new discoveries could open up new possibilities for the creation of effective bifunctional catalysts for urea-assisted hydrogen production.

CRediT authorship contribution statement

Xiaocheng Xu: Methodology, Validation, Investigation, Data curation, Writing – original draft. **Haijun Liao:** Data curation, DFT calculation, Visualization. **Le Huang:** DFT calculation, Validation. **Sijie Chen:** Validation, Investigation, **Rui Wang:** Validation, Resources. **Sheng Wu:** Validation, Resources. **Yanxue Wu:** Resources. **Zhipeng Sun:** Project administration, Writing – review & editing, Funding acquisition, Supervision. **Haitao Huang:** Writing – review & editing, Supervision.

Declaration of Competing Interest

The authors declare that they have no known competing financial interests or personal relationships that could have appeared to influence the work reported in this paper.

Acknowledgments

This work was supported by the Guangdong University of

Technology Hundred Talents Program (No. 220418136), the Shanghai Cooperation Organisation Science and Technology Partnership Program (No. 2020E01020). We would like to thank Analysis and Test Center of Guangdong University of technology for the support of XPS tests. We also would like to thank Shiyanjia Lab (www.shiyanjia.com) for the support of TEM/HRTEM and EPR tests.

Appendix A. Supporting information

Supplementary data associated with this article can be found in the online version at [doi:10.1016/j.apcatb.2023.123312](https://doi.org/10.1016/j.apcatb.2023.123312).

References

- [1] Z.W. Seh, J. Kibsgaard, C.F. Dickens, I.B. Chorkendorff, J.K. Norskov, T. F. Jaramillo, Combining theory and experiment in electrocatalysis: insights into materials design, *Science* 355 (2017), eaad4998, <https://doi.org/10.1126/science.aad4998>.
- [2] Z. He, J. Zhang, Z. Gong, H. Lei, D. Zhou, N. Zhang, W. Mai, S. Zhao, Y. Chen, Activating lattice oxygen in NiFe-based (oxy)hydroxide for water electrolysis, *Nat. Commun.* 13 (2022), 2191, <https://doi.org/10.1038/s41467-022-29875-4>.
- [3] Z.-Y. Yu, Y. Duan, X.-Y. Feng, X. Yu, M.-R. Gao, S.-H. Yu, Clean and affordable hydrogen fuel from alkaline water splitting: past, recent progress, and future prospects, *Adv. Mater.* 33 (2021), 2007100, <https://doi.org/10.1002/adma.202007100>.
- [4] X. Ren, C. Wei, Y. Sun, X. Liu, F. Meng, X. Meng, S. Sun, S. Xi, Y. Du, Z. Bi, G. Shang, A.C. Fisher, L. Gu, Z.J. Xu, Constructing an adaptive heterojunction as a highly active catalyst for the oxygen evolution reaction, *Adv. Mater.* 32 (2020), 2001292, <https://doi.org/10.1002/adma.202001292>.
- [5] X. Li, M. Chen, Y. Ye, C. Chen, Z. Li, Y. Zhou, J. Chen, F. Xie, Y. Jin, N. Wang, H. Meng, Electronic structure modulation of nickel sites by cationic heterostructures to optimize ethanol electrooxidation activity in alkaline solution, *Small* (2023), 2207086, <https://doi.org/10.1002/smll.202207086>.
- [6] X. Peng, X. Nie, L. Zhang, T. Liang, Y. Liu, P. Liu, Y.-L. Men, L. Niu, J. Zhou, D. Cui, Y.-X. Pan, Carbon-coated tungsten oxide nanospheres triggering flexible electron transfer for efficient electrocatalytic oxidation of water and glucose, *ACS Appl. Mater. Interfaces* 12 (2020) 56943–56953, <https://doi.org/10.1021/acsmami.0c13547>.
- [7] J. Li, S. Wang, J. Chang, L. Feng, A review of Ni based powder catalyst for urea oxidation in assisting water splitting reaction, *Adv. Powder Mater.* 1 (2022), 100030, <https://doi.org/10.1016/j.apmate.2022.01.003>.
- [8] D. Zhu, H. Zhang, J. Miao, F. Hu, L. Wang, Y. Tang, M. Qiao, C. Guo, Strategies for designing more efficient electrocatalysts towards the urea oxidation reaction, *J. Mater. Chem. A* 10 (2022) 3296–3313, <https://doi.org/10.1039/DITA09989B>.
- [9] B. Zhu, Z. Liang, R. Zou, Designing advanced catalysts for energy conversion based on urea oxidation reaction, *Small* 16 (2020) 1906133.
- [10] R. Lin, L. Kang, T. Zhao, J. Feng, V. Celorio, G. Zhang, G. Cibin, A. Kucernak, D.J. L. Brett, F. Corà, I.P. Parkin, G. He, Identification and manipulation of dynamic active site deficiency-induced competing reactions in electrocatalytic oxidation processes, *Energy Environ. Sci.* 15 (2022) 2386–2396, <https://doi.org/10.1039/D1EE03522C>.
- [11] L. Yuan, S. Liu, S. Xu, X. Yang, J. Bian, C. Lv, Z. Yu, T. He, Z. Huang, D. W. Boukhvalov, C. Cheng, Y. Huang, C. Zhang, Modulation of Volmer step for efficient alkaline water splitting implemented by titanium oxide promoting surface reconstruction of cobalt carbonate hydroxide, *Nano Energy* 82 (2021), 105732, <https://doi.org/10.1016/j.nanoen.2020.105732>.
- [12] Z. Duan, D. Zhao, Y. Sun, X. Tan, X. Wu, Bifunctional Fe-doped CoP@Ni₂P heteroarchitectures for high-efficient water electrocatalysis, *Nano Res.* 15 (2022) 8865–8871, <https://doi.org/10.1007/s12274-022-4673-z>.
- [13] X. Xu, C. Zhang, J. Li, H. Liu, G. Su, Z. Shi, M. Huang, Redistributing interfacial charge density of Ni₁₂P₃/Ni₃P via Fe doping for ultrafast urea oxidation catalysis at large current densities, *Chem. Eng. J.* 452 (2023), 139362, <https://doi.org/10.1016/j.cej.2022.139362>.
- [14] W.-Y. Fu, Y.-X. Lin, M.-S. Wang, S. Si, L. Wei, X.-S. Zhao, Y.-S. Wei, Sepaktakraw-like catalyst Mn-doped CoP enabling ultrastable electrocatalytic oxygen evolution at 100 mA·cm⁻² in alkali media, *Rare Met.* 41 (2022) 3069–3077, <https://doi.org/10.1007/s12598-022-02006-0>.
- [15] X. Zhang, X. Yin, Z. Song, K. Zhu, D. Cao, J. Yao, G. Wang, Q. Yan, Peony-like Cu_xS_y hybrid iron-nickel sulfide heterogeneous catalyst for boosting alkaline oxygen evolution reaction, *Surf. Interfaces* 38 (2023), 102788, <https://doi.org/10.1016/j.surfin.2023.102788>.
- [16] X. Zhang, Z. Song, Q. Yan, W. Cong, L. Yang, K. Zhu, K. Ye, J. Yan, D. Cao, G. Wang, Tremella-like manganese dioxide complex (Fe,Ni)₃S₄ hybrid catalyst for highly efficient oxygen evolution reaction, *J. Power Sources* 515 (2021), 230627, <https://doi.org/10.1016/j.jpowsour.2021.230627>.
- [17] X. Liu, H. Qin, G. Wang, Q. Li, Q. Huang, Z. Wen, S. Mao, Co-doped Ni-Mo oxides: highly efficient and robust electrocatalysts for urea electrooxidation assisted hydrogen production, *J. Mater. Chem. A* 10 (2022) 16825–16833, <https://doi.org/10.1039/D2TA04728D>.
- [18] Z.-Y. Yu, C.-C. Lang, M.-R. Gao, Y. Chen, Q.-Q. Fu, Y. Duan, S.-H. Yu, Ni-Mo-O nanorod-derived composite catalysts for efficient alkaline water-to-hydrogen conversion via urea electrolysis, *Energy Environ. Sci.* 11 (2018) 1890–1897.
- [19] X. Xu, J. Li, C. Zhang, S. Zhang, G. Su, Z. Shi, H. Wang, M. Huang, Controllable transition engineering from homogeneous NiSe₂ nanowrinkles to heterogeneous Ni₃Se₄/NiSe₂ rod-like nanoarrays for promoted urea-rich water oxidation at large current densities, *Appl. Catal. B* 319 (2022), 121949, <https://doi.org/10.1016/j.apcatb.2022.121949>.
- [20] X. Xu, R. Wang, S. Chen, A. Trukhanov, Y. Wu, L. Shao, L. Huang, Z. Sun, Interface engineering of hierarchical P-doped NiSe/2H-MoSe₂ nanorod arrays for efficient hydrogen evolution, *Inorg. Chem. Front.* 9 (2022) 5507–5516, <https://doi.org/10.1039/D2QI01498J>.
- [21] J. Li, S. Wang, S. Sun, X. Wu, B. Zhang, L. Feng, A review of hetero-structured Ni-based active catalysts for urea electrolysis, *J. Mater. Chem. A* 10 (2022) 9308–9326, <https://doi.org/10.1039/D2TA00120A>.
- [22] H. Liu, S. Zhu, Z. Cui, Z. Li, S. Wu, Y. Liang, Ni₂P nanoflakes for the high-performing urea oxidation reaction: linking active sites to a UOR mechanism, *Nanoscale* 13 (2021) 1759–1769, <https://doi.org/10.1039/DONR08025J>.
- [23] Z. Ji, Y. Song, S. Zhao, Y. Li, J. Liu, W. Hu, Pathway manipulation via Ni, Co, and V ternary synergism to realize high efficiency for urea electrocatalytic oxidation, *ACS Catal.* 12 (2022) 569–579, <https://doi.org/10.1021/acscatal.1c05190>.
- [24] Z. Xu, Q. Chen, Q. Chen, P. Wang, J. Wang, C. Guo, X. Qiu, X. Han, J. Hao, Interface enables faster surface reconstruction in a heterostructured Co-Ni-S electrocatalyst towards efficient urea oxidation, *J. Mater. Chem. A* 10 (2022) 24137–24146, <https://doi.org/10.1039/D2TA05494A>.
- [25] Y. Zhou, B. Chu, Z. Sun, L. Dong, F. Wang, B. Li, M. Fan, Z. Chen, Surface reconstruction and charge distribution enabling Ni/W₅N₄ Mott-Schottky heterojunction bifunctional electrocatalyst for efficient urea-assisted water electrolysis at a large current density, *Appl. Catal. B* 323 (2023), 122168, <https://doi.org/10.1016/j.apcatb.2022.122168>.
- [26] Y. Zeng, M. Zhao, Z. Huang, W. Zhu, J. Zheng, Q. Jiang, Z. Wang, H. Liang, Surface reconstruction of water splitting electrocatalysts, *Adv. Energy Mater.* 12 (2022), 2201713, <https://doi.org/10.1002/aenm.202201713>.
- [27] B. Dong, M.-X. Li, X. Shang, Y.-N. Zhou, W.-H. Hu, Y.-M. Chai, Surface reconstruction through cathodic activation of first-row transition metal phosphides for enhanced hydrogen evolution, *J. Mater. Chem. A* 10 (2022) 17477–17487, <https://doi.org/10.1039/D2TA05293H>.
- [28] C. Gu, G. Zhou, J. Yang, H. Pang, M. Zhang, Q. Zhao, X. Gu, S. Tian, J. Zhang, L. Xu, Y. Tang, NiS/MoS₂ Mott-Schottky heterojunction-induced local charge redistribution for high-efficiency urea-assisted energy-saving hydrogen production, *Chem. Eng. J.* 443 (2022), 136321, <https://doi.org/10.1016/j.cej.2022.136321>.
- [29] C. Li, Y. Liu, Z. Zhuo, H. Ju, D. Li, Y. Guo, X. Wu, H. Li, T. Zhai, Local charge distribution engineered by schottky heterojunctions toward urea electrolysis, *Adv. Energy Mater.* 8 (2018), 1801775, <https://doi.org/10.1002/aenm.201801775>.
- [30] C. Wang, H. Lu, Z. Mao, C. Yan, G. Shen, X. Wang, Bimetal Schottky heterojunction boosting energy-saving hydrogen production from alkaline water via urea electrocatalysis, *Adv. Funct. Mater.* 30 (2020), 2000556, <https://doi.org/10.1002/adfm.202000556>.
- [31] K. Ji, J. Wang, P. Yang, NiCo nanolayered double hydroxides on Fe/Ni metal-organic frameworks for oxygen evolution, *ACS Appl. Nano Mater.* 6 (2023) 7931–7941, <https://doi.org/10.1021/acsnano.3c01138>.
- [32] H. N Dhandapani, A. Karmakar, S.S. Selvasundarasekar, S. Kumaravel, S. Nagappan, R. Madhu, B. Ramesh Babu, S. Kundu, Modulating the surface electronic structure of active Ni sites by engineering hierarchical NiFe-LDH/CuS over Cu foam as an efficient electrocatalyst for water splitting, *Inorg. Chem.* 61 (2022) 21055–21066, <https://doi.org/10.1021/acs.inorgchem.2c03589>.
- [33] M. Gu, L. Jiang, S. Zhao, H. Wang, M. Lin, X. Deng, X. Huang, A. Gao, X. Liu, P. Sun, X. Zhang, Deciphering the space charge effect of the p-n junction between copper sulfides and molybdenum selenides for efficient water electrolysis in a wide pH range, *ACS Nano* 16 (2022) 15425–15439, <https://doi.org/10.1021/acsnano.2c07255>.
- [34] D. Xu, S.-N. Zhang, J.-S. Chen, X.-H. Li, Design of the synergistic rectifying interfaces in Mott-Schottky catalysts, *Chem. Rev.* 123 (2023) 1–30, <https://doi.org/10.1021/acscchemrev.2c00426>.
- [35] A. El Jaouhari, A. Slassi, B. Zhang, A. Pershin, W. Liu, D. Cornil, X. Liu, J. Zhu, The role of selenium vacancies in the enhancement of electrocatalytic activity of CoNiSe₂ for the oxygen evolution reaction, *J. Power Sources* 514 (2021), 230596, <https://doi.org/10.1016/j.jpowsour.2021.230596>.
- [36] F. Yue, C. Wang, W. Duan, H. Pang, T. Wei, K. Xue, D. Wang, F. Fu, C. Yang, Selenium vacancies regulate d-band centers in Ni₃Se₄ toward paired electrolysis in anion-exchange membrane electrolyzers for upgrading N-containing compounds, *Sci. China Chem.* 66 (2023) 2109–2120, <https://doi.org/10.1007/s11426-023-1636-7>.
- [37] J. Li, X. Xu, X. Hou, S. Zhang, G. Su, W. Tian, H. Wang, M. Huang, A. Toghan, Interface engineering of NiSe₂ nanowrinkles/Ni5P4 nanorods for boosting urea oxidation reaction at large current densities, *Nano Res.* 16 (2023) 8853–8862, <https://doi.org/10.1007/s12274-023-5575-4>.
- [38] Y. Shi, W. Du, W. Zhou, C. Wang, S. Lu, S. Lu, B. Zhang, Unveiling the promotion of surface-adsorbed halogenate on the electrocatalytic oxygen evolution reaction, *Angew. Chem. Int. Ed.* 59 (2020) 22470–22474.
- [39] L. Zhou, C. Yang, W. Zhu, R. Li, X. Pang, Y. Zhen, C. Wang, L. Gao, F. Fu, Z. Gao, Y. Liang, Boosting alkaline hydrogen evolution reaction via an unexpected dynamic evolution of molybdenum and selenium on MoSe₂ electrode, *Adv. Energy Mater.* (2022), 2202367, <https://doi.org/10.1002/aenm.202202367>.
- [40] Y. Li, Y. Zhang, X. Tong, X. Wang, L. Zhang, X. Xia, J. Tu, Recent progress on the phase modulation of molybdenum disulphide/diselenide and their applications in electrocatalysis, *J. Mater. Chem. A* 9 (2021) 1418–1428, <https://doi.org/10.1039/D0TA08514F>.

- [41] A. Sobhani, M. Salavati-Niasari, Transition metal selenides and diselenides: hydrothermal fabrication, investigation of morphology, particle size and and their applications in photocatalyst, *Adv. Colloid Interface Sci.* 287 (2021), 102321, <https://doi.org/10.1016/j.cis.2020.102321>.
- [42] S. Ni, H. Qu, Z. Xu, X. Zhu, H. Xing, L. Wang, J. Yu, H. Liu, C. Chen, L. Yang, Interfacial engineering of the NiSe₂/FeSe₂ p-p heterojunction for promoting oxygen evolution reaction and electrocatalytic urea oxidation, *Appl. Catal. B* 299 (2021), 120638, <https://doi.org/10.1016/j.apcatb.2021.120638>.
- [43] Y. Yang, Y. Kang, H. Zhao, X. Dai, M. Cui, X. Luan, X. Zhang, F. Nie, Z. Ren, W. Song, An interfacial electron transfer on tetrahedral NiS₂ /NiSe₂ heterocages with dual-phase synergy for efficiently triggering the oxygen evolution reaction, *Small* 16 (2020), 1905083, <https://doi.org/10.1002/smll.201905083>.
- [44] J. Zhou, L. Yuan, J. Wang, L. Song, Y. You, R. Zhou, J. Zhang, J. Xu, Combinational modulations of NiSe₂ nanodendrites by phase engineering and iron-doping towards an efficient oxygen evolution reaction, *J. Mater. Chem. A* 8 (2020) 8113–8120, <https://doi.org/10.1039/DOTA00860E>.
- [45] F. Zhang, R. Zhao, Y. Wang, L. Han, J. Gu, Z. Niu, Y. Yuan, N. Qu, J. Meng, D. Wang, Superwettable surface-dependent efficiently electrocatalytic water splitting based on their excellent liquid adsorption and gas desorption, *Chem. Eng. J.* 452 (2023), 139513, <https://doi.org/10.1016/j.cej.2022.139513>.
- [46] Y. Liang, Y. Han, J. Li, J. Wang, D. Liu, Q. Fan, Wettability control in electrocatalyst: a mini review, *J. Energy Chem.* 70 (2022) 643–655, <https://doi.org/10.1016/j.jechem.2021.09.005>.
- [47] J. Yu, K. Hu, Z. Zhang, L. Luo, Y. Liu, D. Zhou, F. Wang, Y. Kuang, H.J. Xu, H. Li, H. Duan, X. Sun, Interfacial nanobubbles' growth at the initial stage of electrocatalytic hydrogen evolution, *Energy Environ. Sci.* 16 (2023) 2068–2079, <https://doi.org/10.1039/D2EE04143J>.
- [48] J.N. Hausmann, P.W. Menezes, Why should transition metal chalcogenides be investigated as water splitting precatalysts even though they transform into (oxyhydr)oxides? *Curr. Opin. Electrochem.* 34 (2022), 100991 <https://doi.org/10.1016/j.coelec.2022.100991>.
- [49] M. Ning, F. Zhang, L. Wu, X. Xing, D. Wang, S. Song, Q. Zhou, L. Yu, J. Bao, S. Chen, Z. Ren, Boosting efficient alkaline fresh water and seawater electrolysis via electrochemical reconstruction, *Energy Environ. Sci.* 15 (2022) 3945–3957, <https://doi.org/10.1039/D2EE01094A>.
- [50] H. Liao, X. Zhang, S. Niu, P. Tan, K. Chen, Y. Liu, G. Wang, M. Liu, J. Pan, Dynamic dissolution and re-adsorption of molybdate ion in iron incorporated nickel-molybdenum oxyhydroxide for promoting oxygen evolution reaction, *Appl. Catal. B* 307 (2022), 121150, <https://doi.org/10.1016/j.apcatb.2022.121150>.
- [51] A. Majumdar, P. Dutta, A. Sikdar, H. Lee, D. Ghosh, S.N. Jha, S. Tripathi, Y. Oh, U. N. Maiti, Impact of atomic rearrangement and single atom stabilization on MoSe₂ @NiCo₂Se₄ heterostructure catalyst for efficient overall water splitting, *Small* 18 (2022), 2200622, <https://doi.org/10.1002/smll.202200622>.
- [52] Y.-J. Tang, Y. Wang, K. Zhou, In situ oxidation transformation of trimetallic selenide to amorphous FeCo-oxyhydroxide by self-sacrificing MoSe₂ for efficient water oxidation, *J. Mater. Chem. A* 8 (2020) 7925–7934, <https://doi.org/10.1039/C9TA14133B>.
- [53] Y. Song, M. Sun, S. Zhang, X. Zhang, P. Yi, J. Liu, B. Huang, M. Huang, L. Zhang, Alleviating the work function of vein-like Co_xP by Cr doping for enhanced seawater electrolysis, *Adv. Funct. Mater.* (2023), 2214081, <https://doi.org/10.1002/adfm.202214081>.
- [54] X. Zhang, Y. Xue, X. Yin, L. Shen, K. Zhu, X. Huang, D. Cao, J. Yao, G. Wang, Q. Yan, Defect-rich Mn_xO_y complex Fe–Ni sulfide heterogeneous electrocatalyst for a highly efficient hydrogen evolution reaction, *J. Power Sources* 540 (2022), 231664, <https://doi.org/10.1016/j.jpowsour.2022.231664>.
- [55] Y. Jin, S. Huang, X. Yue, H. Du, P.K. Shen, Mo- and Fe-modified Ni(OH)₂/NiOOH nanosheets as highly active and stable electrocatalysts for oxygen evolution reaction, *ACS Catal.* 8 (2018) 2359–2363, <https://doi.org/10.1021/acscatal.7b04226>.
- [56] L. Wei, M. Du, R. Zhao, F. Lv, L. Li, L. Zhang, D. Zhou, J. Su, High-valence Mo doping for highly promoted water oxidation of NiFe (oxy)hydroxide, *J. Mater. Chem. A* 10 (2022) 23790–23798, <https://doi.org/10.1039/D2TA05600C>.
- [57] F. Zhang, X. Wang, W. Han, Y. Qian, L. Qiu, Y. He, L. Lei, X. Zhang, The synergistic activation of Ce-doping and CoP/Ni₃P hybrid interaction for efficient water splitting at large-current-density, *Adv. Funct. Mater.* 33 (2023), 2212381, <https://doi.org/10.1002/adfm.202212381>.
- [58] L. Su, D. Gong, N. Yao, Y. Li, Z. Li, W. Luo, Modification of the intermediate binding energies on Ni/Ni₃N heterostructure for enhanced alkaline hydrogen oxidation reaction, *Adv. Funct. Mater.* 31 (2021), 2106156, <https://doi.org/10.1002/adfm.202106156>.
- [59] S. Jiao, X. Fu, H. Huang, Descriptors for the evaluation of electrocatalytic reactions: d-band theory and beyond, *Adv. Funct. Mater.* 32 (2022), 2107651, <https://doi.org/10.1002/adfm.202107651>.
- [60] S. Sun, X. Zhou, B. Cong, W. Hong, G. Chen, Tailoring the d-band centers endows (Ni_xFe_{1-x})₂P nanosheets with efficient oxygen evolution catalysis, *ACS Catal.* 10 (2020) 9086–9097, <https://doi.org/10.1021/acscatal.0c01273>.